A gradient in inner pressure of germline cells controls overlaying epithelial cell morphogenesis

Laurie-Anne Lamiré[1,3], Pascale Milani[1,3], Gaël Runel[1], Annamaria Kiss[2], Leticia Arias[1], Blandine Vergier[1], Pradeep Das[2], David Cluet[1], Arezki Boudaoud[2] and Muriel Grammont[1]

[1]Univ Lyon, ENS de Lyon, CNRS UMR 5239, INSERM U1210, Laboratoire de Biologie et de Modélisation de la Cellule, 15, Parvis Rene Descartes, F-69007, Lyon, France.
[2]Reproduction et Développement des Plantes, Univ Lyon, ENS de Lyon, UCB Lyon 1, CNRS, INRA, 15, Parvis Rene Descartes, F-69007, Lyon, France.

[3]These authors contributed equally to this work

Correspondence should be addressed to A.B. and M.G., and to D. C. for the FindCurve ImageJ macro.
arezki.boudaoud@ens-lyon.fr ; muriel.grammont@ens-lyon.fr
david.cluet@ens-lyon.fr

Tel: 33 4 72 72 88 73

Running Title: Cytoplasmique pressure in morphogenesis

Key Words: Cytoplasmic pressure, epithelial morphogenesis, *Drosophila*

Abstract

How internal tissue growth impacts on surrounding epithelium is unknown. To address this, we used the *Drosophila* ovarian follicle, which is composed of a cluster of 15 anterior nurse cells and one oocyte, surrounded by epithelial cells. While the nurse cells grow, the epithelial cells covering them flatten progressively in anterior. We demonstrated that a gradient of cytoplasmic pressure, from anterior to posterior, is present in the nurse cells and that this gradient controls the timing and the wave of the epithelial cell flattening, by acting on TGFß. Our data indicate that intrinsic nurse cell growth is important to control nurse cell pressure. Finally, we revealed that nurse cell pressure, and subsequent TGFß activity, lead to enhanced follicle elongation in anterior and this is crucial to maintain nurse cell integrity. Cytoplasmic pressure is thus essential to shape autonomously and non-autonomously the cells during development.

Introduction:

To build organs, epithelial cells adopt collectively specific shapes. Over the last four decades, it has been demonstrated that cell and organ morphogenesis depend on the integration of extrinsic and intrinsic biological cues (endocrine, paracrine or autocrine signalling; cell-cell or cell-extracellular matrix adhesion; actin filament and microtubule organisation…). More recently, by deciphering the regulation of the acto-myosin network activity, significant findings on cell shape changes during development have been made (Fischer et al., 2009; Heer and Martin, 2017; Michael and Yap, 2013; Pilot et al., 2006; Quintin et al., 2008; Xu et al., 2011). These studies shed light on the importance of considering the mechanical properties of the cells to understand morphogenesis (Farge, 2003; Janmey et al., 2007; Kasza et al., 2007; Mammoto and Ingber, 2010) However, cell shape is not only imposed by the intrinsic forces generated by the cytoskeleton and transmitted through adherens junction or cell-extracellular matrix contacts (Daley and Yamada, 2013; Etournay et al., 2015; Farhadifar et al., 2007; Hoffman and Yap, 2015; Martin et al., 2009; Ng et al., 2014; Rauzi et al., 2008; Taylor- Weiner et al., 2015). It also depends on the cytoplasmic pressure of the cells, and so far, virtually no study paid attention to this physical component and to its role in counter-balancing cortical tension and imposing cell shape. In addition, cytoplasmic pressure of a cell may also impact and deform neighbouring cells. Nevertheless, the implication in development of such extrinsic mechanical forces, due to neighbouring cells, is far less investigated and known, compared to intrinsic forces (Butler et al., 2009; Hiramatsu et al., 2013).

With its simple structure and its well-characterized pattern of development, the *Drosophila* ovarian follicle is a valuable model to study epithelial cell morphogenesis. A follicle consists of an inner cyst of 16 germinal cells (15 nurse cells and one posteriorly-localized oocyte) surrounded by a monolayered epithelium of about 800 cells, which are themselves covered by an outer basement membrane (BM) (Figure 1A). Follicle development has been divided in 14 stages with stages 1 and 14 corresponding to a follicle emerging from the germarium and a mature egg, respectively (King, 1970; Spradling., 1993). The follicle is initially small and spherical with a 10 µm diameter. The growth of the germline cells occurs progressively until S8 before undergoing a major increase. The germline cells are connected to each other through ring canals (RC) and these are used to transfer nurse cell (NC) cytoplasmic contents into the oocyte (Robinson et al., 1994). This transfer leads to the

progressive enlargement of the oocyte relative to individual NCs from S9 onwards. In parallel, the epithelial cells accommodate the germline growth by first proliferating to reach about 850 cells from S1 to S6 and second by increasing in volume and change of shape from S7 to S14 (King, 1970; Spradling., 1993). Epithelial shape changes start at S9. Starting from a cuboidal shape, about fifty cells, called the stretched cells (StCs), flatten above the nurse cells while the others, called the main body follicular cells (MBFC), become columnar above the oocyte. StC flattening occurs progressively from the anterior to the middle of the follicle. This morphogenetic process depends on the activation of a genetic program in the StCs, such as the TGFß pathway and the *tao* gene, which control the remodelling of the adherens junctions (AJ) and the lateral adhesion complexes, respectively (Brigaud et al., 2015; Gomez et al., 2012; Grammont, 2007). The remodelling consists of a stereotypical AJ disassembly with first remodelling of the vertexes of the cells located on the same row and then the AJ perpendicular to the antero-posterior axis (A/P). The AJ parallel to the AP axis elongate while the vertices of the cells of the next row start remodelling. Finally, disassembly of the AJ parallel to the AP axis, occurs at late S9, leading to absence of visible AJs at S10 (Figure 1B). Cell flattening also comes with changes in BM mechanical properties and interactions, which are both controlled by the TGFß pathway (Chlasta et al., 2017). In addition, StC flattening depends on the growth of the germline cells that controls the degree of StCs (Kolahi et al., 2009). How this external force influences StC flattening has never been investigated.

In this study, we established that an A/P gradient of pressure is present in the NCs and demonstrated that this gradient is responsible for the progressive change of shape of the StCs by controlling TGFß expression. Our data present evidence that pressure level is modulated by intrinsic NC growth, and by the pattern and the size of the RCs. We revealed that NC inner pressure leads to inhomogeneous follicle expansion, with a bias toward the anterior and that this anterior expansion requires StC flattening and/or BM softening. Finally, this expansion is crucial for the maintenance of NC integrity as their inner pressure builds up.

Results

The wave of StC flattening do not solely depend on TGFß activity

StC flattening occurs like a wave from anterior to posterior and depends on TGFß signalling. We quantified the expression of the phosphorylated form of Mad (pMad), which indicates TGFß activity, during StC flattening and confirmed that the pathway is activated as a wave during the process (Figure 1C-E). To test whether the spatio-temporal pattern of TGFß is solely responsible of the progressive change of shape, we quantified StCs apical surface expressing an active and constitutive form of the TGFß receptor Thickvein (Tkv), which we refer as TkvA. Our data show that the TkvA-expressing StCs still flatten as a wave from anterior to posterior, demonstrating that providing ubiquitously TGFß activity is not sufficient to induce simultaneous and homogenous cell flattening (Figure 1F, G). Another parameter, than the TGFß activity pattern, must control the wave of flattening.

An antero-posterior gradient of cytoplasmic pressure is present within the nurse cells

By examining the NC membrane shape, we observed that some membranes bulge out toward the posterior at S9 and that this bulging is stronger between anterior NCs than between posterior NCs (Figure 1H). We confirmed this by measuring the radii of circles fitting the curvatures in fixed tissues (Figures 1I and S1A, S1B). These data suggest that a gradient of cytoplasmic pressure exists in the NC compartment with more pressurized NCs in anterior. This led us to hypothesize that the NC inner gradient could be responsible for the wave of the StC flattening.

To assess and measure the NC cytoplasmic pressure, we developed three methods. First, we generated 3D reconstructions from live follicles to be more accurate than 2D measurements (Movie 1). This was performed by using multi-angle image acquisition, three-dimensional reconstruction and cell segmentation (MARS) (Fernandez et al., 2010) (Figure S1C-F). We then developed an Image J macro that automatically measures individual NC membrane curvature (See STAR methods). The macro selects the slice with the widest area along the x, y or z axis (Fig S2A), identifies the number of corners, draws the corresponding polygon and determines the best circles fitting the different segments and calculates the curvature radii. The direction of the curvature (concave, convex or flat) is given by comparing the position of the circle with the polygon. We observed that the posterior NC membranes

become progressively convex from S7 to S9, and this is correlated with the anterior NC membranes becoming concave (Figures 1J, K and S2B, S2C, S2E). At S9, 72 % of the membranes facing the posterior are convex compare to 3% of the membranes facing the anterior, indicating that NCs are bulging toward the posterior. This is also true for the four posterior NC that bulge in the oocyte (Movie2), indicating that the oocyte pressure is lower than the NC. No specific orientation is ever observed for the lateral membranes (Figure S2F). Surprisingly, the anterior membranes of the oocyte, switch from convex to concave between stages 5 to S9, suggesting that the oocyte is first pressurized before being deformed by the inner pressure of the posterior NCs (Fig S2D, S2G). Thus, the direction of the membrane curvature supports the presence of the gradient of cytoplasmic pressure at S8 and S9.

Second, as cytoplasmic pressure contributes to tissue stiffness, we used an Atomic Force Microscope (AFM), a standard approach to measure non-invasively stiffness of biological samples (Beauzamy et al., 2015; Kim et al., 2014; Milani et al., 2014). The stiffness quantifies how easily a body is deformed when a force is applied to it; a high value corresponds to a stiff material. Living follicles are dissected as described in Chlasta *et al*. (2017) (Figure S3A). The measurement of the NC apparent stiffness requires deforming the BM and the follicular cells. We previously established that BM height is on average 0.2 µm and FC height changes from about 5 µm before the S9 to less than 1 µm after flattening (Kolahi et al., 2009). Since AFM measurements typically allow a maximum of 3-4 µm indentations, we could not probe NCs prior to S9 (Figure S3B). During S9, one, two or three areas, located above the anterior, central or posterior parts of the NCs, respectively, are probed depending on the progression of the flattening (Figure S3C). The stiffness of the cantilever and the force applied were chosen to enable indentation depths of 1.5 to 2.5 µm, which is more than the height of the BM and the flattened StCs. To perform the measurements, we used the Contact mode (Ramp module) of the AFM, and registered 100 raw force curves from a 10 x 10 matrix, with indentation points spaced 100 nm apart. From the force curves, we first quantified the apparent stiffness along the follicle (Figure S2D). In parallel, we quantified the curvature of the follicle surface at the measurement points. With the values of indentation depth used, we extracted pressure following the protocol developed by Beauzamy et al., (2015); the pressure being deduced from stiffness and curvature (Figure S3E) (see Methods). We observed that the inner pressure of the anterior NCs increases by a factor of 3 during

StC flattening and that an antero-posterior gradient of pressure is present with the highest pressure in the most anterior probed area (Figure 2A, B and S4A). We note that the measurements referred to as “anterior” were not necessarily performed on the most anterior cell for each follicle, as the curvature of the follicle can sometimes prevent access. Although NC pressure displays a broad range of values, from about 100 Pa to 450 Pa, variation between the different areas of a same follicle is by a factor of 1.2 to 1.5 (Figure S4A), compared to the negligible variations detected within each small probed area (Figure S4B, S4C). We note that the values of pressure measured are comparable to those obtained in mitotic cells (Stewart et al. 2011). To confirm that our measurements reflect inner pressure, we performed an osmotic treatment by adding 1M NaCl and observed a sharp decrease of pressure (n=8) (Figure S4D, S4E).

Third, we previously observed that collagenase treatment on follicles leads to the bulging of the NCs toward the outside, as they are not constrained by the basement membrane anymore (Figure 2C) (Chlasta et al.). The radius of the circle fitting the curvature of the NC membrane facing the outside is related to the NC pressure and the cortical tension. We observed that the radii of NCs increase along the antero-posterior axis (Figure 2D). If we consider that the cortical tension of the NCs is similar for all the NCs, these data indicate a gradient of pressure along the A/P axis. To test whether differences in cortical tension between the NCs are negligible or not, we performed AFM measurements on some of these collagenase-treated follicles (Fig 2C). The antero-posterior gradient of pressure is still detected, although the pressures are less elevated than in untreated follicles, possibly due to NC expansion (Fig 2C, E). We also observed an inverse correlation between the pressure and the radii, implying that NC cortical tension does not vary significantly from one NC to the next (Fig S3F). Altogether, the results after collagenase treatment confirm the presence of a gradient within the NC compartment.

The gradient of cytoplasmic pressure controls the wave of StC flattening

To test whether the pressure and the gradient of cytoplasmic pressure is important for the wave of cell flattening, we used the *dicephalic* (*dic*) and *kelch* (*kel*) mutants, which both affect specifically germline development. We expected that *dic* mutation, which decreases the germline growth, would lead to a decrease of pressure whereas *kel* mutation, which prevents the cytoplasmic transfer between the

NCs and the oocyte due to abnormal RC formation, would direct an increase of pressure. AFM measurements show that the pressure is much lower in *dic* follicles than in WT follicle in S10 follicles whereas it is higher than WT for *kel* follicles. In *dic* follicles, the gradient in pressure is not present anymore (Figure 3A-C). In *kel*, a difference between anterior and more posteriorly localised NCs is still detected, but the measurements are more variable, compared to WT. The analysis of the NC membranes curvature showed that only half of the membranes are still bulging toward the posterior in *dic* follicles whereas the they are all convex in *kel* follicles (Figure S5A-D). These data confirm that the gradient of pressure is disrupted in *dic* whereas it is still present in *kel.* These two mutants provide thus valuable mechanical conditions to determine the role of the pressure and of the gradient for StC flattening. StC apical surface quantification shows that no gradient of flattening is present in *dic* follicles (Figure 3D, E, H, S5E, S5F). In contrast, *kel* follicles still display gradual flattening, although it is less pronounced in the central area (Figure 3D, F, H, S5F). We also observed that *kel* follicles present premature flattening, which correlates with the presence of high inner pressure in the anterior NCs at mid-S9 (Figure 3G, I). Altogether, these data demonstrate that the gradient of the NC cytoplasmic pressure controls the wave of StC flatening and that the level of pressure dictates the timing of StC flattening.

The establishment of the gradient of cytoplasmic pressure involves intrinsic NC growth

Inner pressure depends on cortical tension, on protein translation and on fluxes of solutes and of water, all of these contributing to change of cell osmotic pressure and/or volume. Although global NC growth or individual nuclei volume have been already quantified (Alsous et al., 2017; Kolahi et al., 2009), no data provide individual NC volume. With the MARS method (Fernandez et al., 2010), we extracted the precise volume of each NC from S4 to S10 (Figure 4A-F). Our data show that the volume of the NCs between the anterior ones and the central ones is rather similar until S8 and that the oocyte is much smaller than any NC until S7. From S8 onwards, the volume of the germline cells increases dramatically, especially that of the four posterior NCs and of the oocyte (Figure 4G and S6A). This is detected when we observed collectively (Figure 4G) or individually (Figure 4H) the NCs. Indeed, the difference of growth rate between the posterior NCs and the other NCs is of a factor

of 2.2±0.3 (mean ± SD) with the anterior NCs and of 1.8±0.1 with the central NCs between S6 to S10. In contrast, the difference between the anterior NCs and the central NCs is only of a factor of 1.2±0.2. Thus, the posterior NCs grow more dramatically than any other NCs. This leads to the presence of a gradient of volume between the NCs with the anterior NCs being the smallest at S9. No significant differences are observed between all the central cells. The gradient flattens at S10, except for the four posterior NCs. These data demonstrate that NC growth is regulated along the A/P axis during S9.

To determine the importance of NC growth in building up pressure, we first measured the pressure of two NCs with zero entrance ring canals (ERC) localized either in anterior or in contact with the oocyte. The anterior NC always displays a pressure superior to the posterior one (Figure S6B), indicating that intrinsic growth of the NCs is the main parameter to control the NC volume, and therefore pressure. Second, we analysed follicles mutant for *sec5*, encoding a component of the exocyst, which is involved in membrane remodelling (Murthy, 2003). It has been previously shown that the $Sec5^{E13}$ allele leads to major defects in NC membrane trafficking, leading to a progressive breakages of the membranes with syncytial NC. We quantified NC membrane breaks along the A/P axis in follicles with germline clones for $Sec5^{E13}$. In 50 % of S10 follicles, break in NC membranes are observed in the anterior part of the follicle. 10% of the follicles display NC membrane rupture in both the anterior and central areas and in rare cases all the NC membranes were absent (5%, n=20) (Figure 4I), confirming that the presence of an antero-posterior gradient of pressure.

We assumed that the NC membrane breakage would lead to a change in the pressure pattern within the nurse compartment, thus abolishing the A/P gradient of pressure and the wave of StC flattening. To test this, we first analysed StC flattening and observed that adherens junctions remain visible in the StCs located above NC membrane breaks (Figure 4I). Those StCs are smaller than WT and their number increases by a factor of 1.5. Second, we measured the NC curvatures in S9 and S10A follicles with germline clones for $Sec5^{E13}$ (Figure 4J). At S9, before NC membrane breaking occurs, $Sec5^{E13}$ follicles present almost no membranes curving towards the anterior. At S10A when most $Sec5^{E13}$ follicles contains syncytial NCs, we found more than 20 % of the membranes curving towards the anterior with the NCs located around the syncytium bulging towards this cell (Figure 4I). This shows

abnormal pattern in pressure. Third, we measured pressures in flies expressing *Sec5* RNAi specifically in the germline under the control of the MTD-gal4 driver. This genetic condition does not yield to any NC membrane breakage (n=30), suggesting that the inner pressure must be higher than WT but that the NC membrane growth is sufficient to avoid rupture. Our data showed that the NC inner pressure is on average higher than in WT, although it is more variable (Figure 4K). No measure was made on $Sec5^{E13}$ as the probability of getting enough $Sec5^{E13}$ germline clones was too low to allow AFM measurements. Altogether, this demonstrates that NC membrane growth must be controlled to maintain NC inner pressure under a certain threshold, helping them to keep their integrity as pressure increases.

The establishment of the gradient of cytoplasmic pressure depends on cytoplasmic flow between NCs

Our data show that the gradient of pressure is established during S8 until S10A. One important aspect of the NCs is their connection through ring canals (RC) that carry the cytoplasmic fluxes from the NCs to the oocyte (Figure 5A). According to Poiseuille's law, cytoplasmic flux through a RC is proportional to the difference in pressure between the neighbouring NCs and to the ring conductivity. As four synchronous divisions form the whole 16-germline cell cyst, it yields 8 cells with a single RC, four cells with two RC each, and two cells with either three or four RC, one of the latter being the oocyte (Figure 5B). We first analysed the role of the diameter of the RC. It has been previously showed that the RC undergo about a 7-fold increase in diameter throughout the follicle development (Robinson et al., 1994), but no measurements were performed along the anterior-posterior axis. We confirmed that, from S8 to S10, RCs undergo a progressive growth (Figure 5C), but we also observed that a slight gradient of size is present along the A/P axis, with the smallest RC in anterior (Figure 5D). An abrupt increase of the diameter of the 4 RCs connecting the posterior NCs to the oocyte is detected from early S9 onwards. Thus, RC size participate to establishing the gradient of pressure since smaller RCs between anterior NCs and wider RCs between posterior NCs and the oocyte might help building up the pressure in the former and in contrast prevent over-building of pressure in the latter. Secondly, we tested whether the number of entrance RC (ERC) per NC could also be a factor generating different inner pressure. The oocyte has four entrance RCs, each connected to a different posterior NC. Due to the

pattern of cyst formation, the four posterior NCs have, zero, one, two or three ERC (King, 1970). Considering the cytoplasmic flux, we hypothesized that the posterior NC with 3 ERC would have a higher cytoplasmic pressure than the one with no ERC. In 65% of cases, the highest pressure was measured in the cell that has the highest number of ERC (Figure 5E and Figure S6C), indicating that variation in pressure at the same position along the A/P axis can be explained by this parameter. Importantly, the pressure of the NC with three ERC remains always smaller than more anteriorly-localised cells, which in most cases bear zero ERC. The number of ERC cannot be thus considered as responsible of the gradient. It mainly alters the slope (more or less pronounced) of the gradient. This conclusion is also supported by the *kel* phenotype, which shows that partial blocks of the RC does not prevent the establishment of a gradient of pressure.

Inner pressure controls TGFß signalling

Previous work has shown that StC flattening depends on TGFß activity within the StCs and that early activation of TGFß, such as in follicles expressing of a constitutively activated form of the TGFß receptor Thickvein, is sufficient to induce early StC flattening (Brigaud et al., 2015). Our data demonstrate now that StC flattening depends on the NC inner pressure and that StC flattening starts prematurely in case of increased pressure, such as in *kel* follicles. We then searched for whether the Dpp pathway could respond to the NC growth by monitoring and quantifying the level of the phosphorylated form of Mad (pMad), marker of TGFß activity, in *dic* and *kel* follicles. In WT follicles, an antero-posterior gradient of activity become visible early to mid-S9. Then, the amount of pMad decreases in anterior (Figure 1E, 6A, C, D, G). In *dic* follicles, pMad is also detected first in the most anterior area (Figure 6B), but occurs later than in WT. This lower TGFß activity compared to that of WT follicles of a similar size is conserved throughout StC flattening. Additionally, no graded detection of pMad is present between the anterior and the central region in *dic* follicles throughout the S9. In *kel* follicles, pMad is present as early as S7 (Figure 6H). pMad levels is usually stronger by a factor 2 compare to WT and differences between anterior, central and posterior are observed during StC flattening (Figure 6I, J, K). These data show that germline pressure is sufficient to induce TGFß signalling and that in case of low NC pressure, such as in *dic* follicles, another mechanism takes place and allows uniform TGFß activity.

High cytoplasmic pressure, and subsequent StC flattening, leads to enhanced follicle expansion in anterior

Our data show that the anterior NCs are more pressurized than the posterior NCs and than the oocyte. This could force the growing follicle to expand more anteriorly than posteriorly. To test this, we first used fluorescent beads that stick to the BM and analysed the movement of these beads as follicles grow (Fig S7A, S7B). From S8 to S10, we observed that anterior beads shift more anteriorly than the posterior beads shift posteriorly (n=12) (Figures 7A, B, C, and S7C, S7D). Second, we used the *vkg::GFP* line, which expressed one chain of the Collagen IV fused to GFP, resulting in a fluorescent BM. We performed FRAP experiments to locally bleach the GFP contained in the BM in order to generate landmark points (n=5) (Figure 7C). We measured elongation of the anterior and posterior BM segments. On average, the anterior part of the follicles grows 2.5 fold more than the posterior during the S9 (Figure 7D). No significant difference between the anterior and the posterior has been detected in WT S7 or S8 follicles (not shown). In *dic* follicles, the difference between the anterior and the posterior growth is reduced (n=6) (Figure S7E). In parallel, we measured follicle elongation and observed that *dic* follicles do not elongate as much as WT follicles whereas *kel* follicles are more elongated than WT (Figure 7E). In addition, although the rate of elongation is similar between WT and *kel*, it is lower in *dic* compare to WT (Figure 7F). This demonstrates that high inner pressure in NCs biases follicle growth toward the anterior during S9. We then tested whether this anterior follicle expansion requires StC flattening and BM softening by analysing follicle elongation when follicular cells express constitutively Dad, which repress TGFß activity and thus impairs StC flattening and BM softening (Brigaud et al., 2015). Our data show that Dad-expressing follicles expand also less anteriorly and are rounder than WT (Figure 7E, F, G). Importantly, rounder eggs are also laid by females expressing UAS-*dad* in the follicular cells compared to those from WT females (Figure S7F). These data show that anterior follicle expansion, due to high NC inner pressure, requires TGFß activity in the StCs and is important to shape the egg. This lack of elongation could derive from maintenance of a rigid BM in anterior, mechanically preventing elongation. This suggests that NC inner pressure must be high in Dad-expressing follicles. This was confirmed by analysing S10 Dad-expressing follicles that display NC membrane breakage (Figure 7H), especially

between the anterior NCs. This demonstrates that BM softening and StC flattening are important to maintain NC integrity by keeping their pressure under a certain threshold.

Discussion

Mechanical properties of the cells, such as stiffness, are key components of final organ shape. These properties may be important in the cells that form the organ or in neighbouring cells that mechanically impact on the organ, due to the propagation of mechanical stress on long distances. Usually, cell stiffness is considered to be representative of the cortical tension, which depends on the acto-myosin network and on the regulation of its activity. Another factor in stiffness is cytoplasmic pressure, which is counteracted by cortical tension. Here we show that the cytoplasmic pressure in well-defined cells controls the shape changes of surrounding cells. Our data show that this cytoplasmic pressure is regulated in time and in space and influences TGFß expression pattern, whose activity is required in the cells undergoing morphogenesis.

In the *Drosophila* ovarian follicle, StCs flatten as a wave advancing from anterior to posterior above the NCs. In this paper, we demonstrated that an antero-posterior gradient of pressure exists in the NCs from S8 to S10. The WT values for NC inner pressures are in the range observed for other animal tissues, such as chick embryo blastula (10 to 200 Pa) or for cultured cells (Stewart et al., 2011). Usually, the most direct method to measure pressure is the use of a pressure probe. In our system, such a tool could not be used because it would not allow several measurements within a single sample. We tackled this problem by using a combination of non-invasive tools.

Firstly, the atomic force microscope makes it possible to probe underneath tissues in their native environment. In the case of the *Drosophila* ovarian follicle, probing the internal NCs requires deforming the basement membrane and the StCs. Due to indentation range (typically around 3-4 µm), cytoplasmic pressure can be measured in NCs only when StCs have flattened. Importantly, we show that local cell integrity was preserved during experimentation, since no variation in pressure was observed while performing 100 measurements in a given cell. We also demonstrate

the sensitivity of the technique by measuring pressure in different chemical (NaCl treatment, collagenase) or genetic conditions (*dicephalic* and *kelch*).

Secondly, we took advantage of the 3D reconstructions of the germline to infer differential inner pressure between the NCs by measuring the curvature of their membranes. This allowed us to confirm the presence of a gradient, but also to establish that the gradient was already present at S8. In addition, the 3D measurements corroborate 2D measurements of curvature made on fixed and squeezed follicles, opening the possibility to speed up the identification of differential pressure between adjacent cells during any developmental process.

Stiffness depends on inner pressure and on cortical tension, its counterbalancing force. Since it would be uninformative to perform such ablations in follicles, since multiple ablations cannot be carried out in a single follicle, differences in cortical tension along the A/P axis cannot be assessed. Importantly, we detected differences in pressure between anterior and posterior NCs following use of a Myosin inhibitor (not shown), showing that difference in cortical tension is not a major determinant.

Previous studies showed that StC flattening depends on TGFß signalling and on NC growth. Here, by performing measurements in *dicephalic*, we demonstrated that NC inner pressure controls the wave of StC flattening. In parallel, analyses of *kelch* follicles prove that NC inner pressure controls the timing of StC flattening. Importantly, TGFß responds to changes in pressure as its activity is detected late in *dicephalic* and prematurely in *kelch*. Recently, it has been shown that Yorkie, a co-transcriptional activator is present in the StCs (Fletcher et al., 2018). Yki is known to stimulate cell growth with DNA-binding partner proteins. Interestingly, Mad can be one of the Yki partners (Oh and Irvine, 2011). It is also known that Yki can be regulated by cortical tension (Rauskolb et al., 2014). Regulation of StC flattening might thus occur through any or both mechanisms.

Our data show that this gradient remains for about 8 hours (from S8 to mid-S10), suggesting that active mechanisms are needed for its establishment and maintenance. Our data show that three parameters are at play. The first two parameters are the size and the number of RCs. The RCs play a double and opposite function in establishing the gradient pressure. In one hand, they help preventing high pressure in posterior, since the diameter of the RCs between the posterior NCs and the oocyte is bigger than any other rings, facilitating cytoplasmic

transfer in the oocyte. But in the other hand, they increase the pressure in some posteriorly localised NCs, as NCs with one or two ERCs are mainly in the central and posterior areas (Alsous et al., 2017). The third parameter is NC growth. By monitoring NC volume, we demonstrated that difference between anterior and posterior NCs increases during the S9. Our data strongly suggests that any mathematic model for NC growth and the flows between the cells should take into account pressure gradient (Alsous et al.,2017). Finally, our data show the importance of membrane growth to maintain the integrity of the NCs when they grow the most. Surprisingly, although the posterior cells grow more than the anterior ones, the latter are more sensitive to the down-regulation of the exocyst components than the former. Altogether, this suggests that NC growth is not regulated as a function of the pressure, but directly participate to the generation of this pressure.

Several studies have shown the importance of the BM membrane structure and stiffness to elongate the follicle and the egg (Denef et al., 2008; Díaz de la Loza et al., 2017; Haigo and Bilder, 2011; He et al., 2010; Isabella and Horne-Badovinac, 2015, 2016; Lerner et al., 2013; Schneider et al., 2006; Viktorinová and Dahmann, 2013). Two non-exclusive models have been proposed. First, a softer basement membrane at both poles of the follicle would favour expansion along the A/P axis (Crest et al., 2017). Second, the structure of the basement membrane with stiff fibril-like structures oriented perpendicular to the A/P axis would prevent radial expansion (Chlasta et al., 2017). The discovery of a gradient of pressure within the NCs sheds light on another level of regulation that acts from S8 to S10. By showing that the follicle expands more anteriorly than posteriorly during S9 because of the inner NC pressure, and of TGFß expression in the StCs, we now propose the following model. Up to S8, follicles elongate due to the global (pole versus centre) and local (fibrils) differences in basement membrane mechanical properties. From S8, the anterior NCs increase their pressure, induce TGFß in the StCs, which leads to their flattening and the local softening of the basement membrane. On the one hand, StC flattening likely facilitates NC growth, required to build up the pressure, by allowing fast transfer of oxygen and nutriment from the hemolymph. One the second hand, BM softening above the StCs likely helps the increase of NC volume and the maintenance of their inner pressure under a certain threshold. Altogether, these mechanisms, intermingling genetic and mechanic regulations, allow coordination in growth and

shape of two adjacent populations (StCs and NCs), which jointly act on the shape of a third cell, the oocyte.

To conclude, our work highlights the importance of examining growth in cells in close proximity to the studied morphogenetic event and reveals the mechanical role of cytoplasmic pressure in shaping cells and organs.

Methods

Fly stocks and clones generations

Canton S was used as WT; the other fly stocks are: *hts::GFP* (Petrella et al., 2007), *Ecad::GFP* (Huang et al., 2009), *PHPLCγ::GFP* (Compagnon et al., 2009), *P(UAS-tkv^{Q199D})* (referred as TkvA)), *P(UAS-Dad.T*) (Bangi and Wharton, 2006), *traffic jam-Gal4* flies (Li et al., 2003), *dic*^{1} (Lohs-Schardin, 1982), *kelch^{ED1}* (Xue and Cooley, 1993), *sec5^{E13}* FRT40A (Coutelis and Ephrussi, 2007; Murthy, 2003), *sec5^{GLC0167Z}* (Murthy et al., 2010), *String^{EPg30417}*, *tribbles^{EPg35131}* ((Mata et al., 2000) and *vkg^{G454}* (allele containing a GFP protein trap in the Col IV a2 chain Viking that we refer as Coll IV::GFP in the text, Morin et al., 2001). Three maternal drivers were used: *nanos-Gal4::VP16 (Bloomington stock center)*, *Maternal triple driver Gal4* (*MTD-Gal4*): *(P(otu-Gal4::VP16.R)1, w[*]; P(Gal4-nos.NGT)40; P(Gal4::VP16-nos.UTR)CG6325[MVD1])* (Petrella et al., 2007)) *and Maternal-tubulin-Gal4 driver* (*mat-tub-Gal4*)*: y w; P(mat-tub-Gal4)mat67; P(mat-tub-Gal4)mat15* (Bloomington stock center).

Fly stocks were cultured at 25°C on standard food. *sec5^{E13}* clones were generated by Flipase-mediated mitotic recombination on FRT40A chromosome carrying RFP as marker (Golic and Lindquist, 1989; Xu and Rubin, 1993). Ectopic expression of TkvA or Dad were performed by generating Flip-out Gal4 clones in animals carrying the hs-FLP22 and the AyGAL4 UAS-GFP transgenes (Ito et al., 1997) or by crossing with *tj*-Gal4 flies. Flipase expression was induced by heat shocking 3 days-old females at 37.3C for 1 h to generate mutant clones or Flip-out clones. Adult females were fed on abundant yeast diet for 2 to 3 days prior to dissection. Expression of RNAi against *sec5*^{GLC01676} or *String^{EPg30417} or* tribbles^{EPg35131} were driven by *nanos-Gal4::VP16, MTD-Gal4 or mat-tub-Gal4.*

Follicle staining and staging

Ovaries from females were dissected directly into fixative 3 to 4 days after Flipase induction and stained following the protocol described in (Grammont, 2007). To avoid fluctuations of the depth of the follicles that are squeezed by the coverslip, each slide contains 15 ovaries, from which S11 to S14 are removed. After dissection of the follicles, most of the PBS is removed and 20µl of the Imaging medium (PBS/Glycerol (25/75) (v/v)) is added before being covered by a 22/32 mm coverslip. The following antibodies were used: goat anti-GFP (1:1000; Abcam), rat anti-ECad (1:200; Developmental Studies Hybridoma Bank), rabbit anti-pMad (1:200; Nakao et al., 1997), mouse anti-Eya (1:200; Developmental Studies Hybridoma Bank).

The follicles were staged using their full length (Lf), the oocyte length for dic and dad-expressing follicles, and the timing of the different morphogenetic processes occurring at S9 (border cell migration and stretched cell flattening), according to Spradling (1993) and King (1970).

Fluorescent quantifications

Mutant and *viking::GFP*/CyO (which served as a control) flies were mixed before dissection. Both WT and mutant ovaries are thus fixed, stained and mounted together. Mutant and control follicles were discriminated thanks to the specific GFP accumulation in the basement membrane in *vkg::GFP* follicles.

For all images, a projection of all of the z sections in which StC nuclei are visible is made and background was subtracted. Nuclei were individually selected and registered as ROI. For each ROI, the "Area" and the “Integrated density" were quantified. Measurements were also performed in 3 areas located close to nuclei to estimate background and a mean of fluorescent background is calculated. The corrected total nuclei fluorescence (CTNF) for each nuclei is given by using the formula: CTNF = Integrated Density – (Area of selected nuclei X Mean of background fluorescence).

Atomic force microscopy (AFM)

AFM indentation experiments were carried out with a Catalyst Bioscope (Bruker Nano Surface, Santa Barbara, CA) that was mounted on an optical macroscope (MacroFluo, Leica) using an objective (10x objective, Mitutuyo). A Nanoscope V controller and Nanoscope software versions 8.15 and 9.2 were utilized.

All quantitative measurements were performed using nitride cantilevers with silicon pyramidal tips (DNP-10 SCANASYST-FLUID+, Bruker AFM probes, Inc.) with a nominal spring constant of 0.7 N/m and a nominal tip radius of 40 nm. The actual spring constant of cantilevers was measured using the thermal tuning method (Hutter and Bechhoefer, 1993; Lévy and Maaloum, 2002) and ranged from 0.6–0.9 N/m, which was sufficient to indent the sample without damaging it. The deflection sensitivity of cantilevers was calibrated against a clean silicon wafer. Fresh dissected follicles were fixed on a Petri dish coated with poly-L-lysine (0,5mg/ml) and were covered by living medium. Follicles are kept for an hour maximum before being discarded. All experiments were made at room temperature and the standard cantilever holder for operation in liquid was used. The Petri dish was positioned on an XY motorized stage and held by a magnetic clamp. Then, the AFM head was mounted on the stage and an approximated positioning with respect to the cantilever was done using the optical macroscope.

To record force curves, the Ramp module of the Contact mode in fluid was used. With this module, individual force curves are acquired at discrete points chosen using the optical image of the follicle. Each AFM measurement consists of the acquisition of 100 force curves extracted as 10 x 10 matrices with indentation points spaced 100 nm apart.

The pressure was deduced from local follicle stiffness and geometry (Beauzamy et al., 2015; Vella et al., 2012). The local stiffness, k, is derived from the force–indentation curves by fitting to a linear model, using depths between 1 and 2 µm in order to probe the pressure of the NCs while minimizing the influence of the basement membrane and of the stretched cells; the stiffness was obtained in piconewtons per meter (pN/m). The geometry at the indented location was characterized by the radii of curvature R_1 and R_2. Considering the follicle to be approximately a surface of revolution, R_1 is the local radius of curvature of the follicle outline and R_2 is the distance along the normal to the outline of the indented point to the axis of revolution. Radii were measured (in µm) from the optical images (from the macroscope) using ImageJ.

The pressure was then computed using the following equation (Vella et al., 2012):

$$P = k/\pi \; 2R_1R_2/(R_1+R_2),$$

with values in Pascals (Pa). To reduce variability, each experimenter performed WT and mutant measurements and comparisons were made between sets obtained by the same experimenter.

Chemical treatment of the follicles

Collagenase (1000 Units/ml CLSP; Worthington Biochemical Corp) was added to a final volume of 200 µl. The reactions were stopped with 10mM L-Cystein.

Imaging for 3D-reconstruction

The MARS (Multi-angle image Acquisition, three-dimensional Reconstruction and cell Segmentation) pipeline is based on the fusion of several confocal stacks of images, taken with multiple angles, in order to recreate a highly resolutive three-dimensional reconstitution of the object. Segmentation is performed from the fused stack (for details, see Fernandez et al. (2010).

PHPLCγ::GFP follicles were dissected in PBS1X, before being stuck onto an coverslip coated with poly-L-lysine (0,5 mg/ml), which was glued on a Pasteur pipette. The pipette was fixed in a large Petri dish, allowing its rotation in three angles (-30°, 0 and +30°). Z-stacks were taken from the three angles using a 40X, 0.75 NA water-immersion objective of a Zeiss LSM700 confocal microscope (for S4 to mid-9 follicles) or using the 32X, 0.85 NA water-immersion objective and a pulse infrared laser (Chamaleon OPO) of a Zeiss LSM 710 (for thick follicles starting mid-late S9). The follicles were either imaged in living conditions or fixed in a 4% formaldehyde solution and anti-GFP antibodies were used to detect PHPLCγ::GFP expression.

Cell Curvature measurements

2D measurements are performed on fixed ovaries by manually applying circles fitting the curvatures between adjacent NCs at a focal plane allowing border cell visualisation.

3D measurements are performed from segmented NCs generated by the MARS method using a custom-made Image macro, called “Find-Curve”. The Find-Curve macro for the ImageJ program (Schneider et al., 2012) automatically processes all cell stacks contained in a root folder indicated by the user. As the third dimension of the stacks, created by the MARS 3D reconstructions, corresponds to the Z axis, the program generates (X and Y) complementary orthogonal views. The three different views are then independently analysed. Using the “Default” threshold,

derived from the Iso-Data algorithm (Ridler, T.W. Calvard, 1978), the macro identifies the slice with the largest area. An option has been implemented to manually specify the slice to analyse. On this slice, for every point (O) of the perimeter, the angle (OA, OB) is calculated, with A and B two neighbours (10th degree) points, respectively upstream and downstream to O. The determination of local maximal angle values along the perimeter allows identification of the "summits" of the cell. These summits are used to define the various segments of the cell and generate the fitting regular polygon. For all segments, the radius of the best fitting osculating circle is calculated (Berutti et al., 2012; Mesmoudi et al., 2010). This value is the curvature radius ρ of the studied segment. Finally, a .html report file is automatically created for human quality control.

A folder, called "test stacks for figure 1J", containing the three stacks corresponding to the nurse cells presented in Figure 1J and the macro can be downloaded by following this link: https://github.com/LBMC/FIND-CURVE

Flow velocity measurements

Flies are dissected in PBS 1X and placed in a petri dish coated with poly-L-lysine and incubated 10 minutes with fluorescent beads (Fluoresbrite® Multifluorescent Microspheres 1.00µm 2,5% (Polysciences Inc.), dilution 1/100) before being rinsed and maintained in the living medium described in Montell. Images are acquired with Leica Macrofluo Plan Apo 5.0X/0.50 LWD objective. Stacks of images (z = 80 µm) were taken each 30 minutes and analysed with the ImageJ plugin, https://sites.google.com/site/qingzongtseng/piv, as described in Tseng et al. (2012). The anterior, central and posterior areas are defined by dividing the length of the follicle.

Basement membrane photobleaching

Homozygous flies for *vkg::GFP* were dissected and maintained in the living medium described in Prasad and Montell (2007). Follicles were placed in a coverslip coated with poly-L-lysine, which was glued to the bottom of a custom-made open chamber. Living medium was added from the top and covered by semipermeable membrane. Fluorescent images of the samples were acquired on an inverted Zeiss LSM 710 confocal microscope with 40x/0,75 water-immersion objective using the 488 nm line of an Argon Laser at 25°C. All images were acquired at a 512 pixel × 512

pixel resolution. FRAP experiments were carried out by scanning over 20µm the follicle starting at about 15 µm from the coverslip. z-sections were performed with a step of 1 µm. The size of bleached region of interest (ROI) was about 10 x 10 x 10 µm, centred within the 20 µm-sized scanned area. Significant bleaching occurs after 20 iterations. All images were acquired at a scan speed of 4. Stacks of images were taken each 30 minutes over 2 hours.

Acknowledgments

We thank DSHB and Bloomington Stock Center for flies and reagents. We thank Lyon Multiscale Imaging Center' (LyMiC) and Arthrotools of the SFR Bioscience (UMS3444/US8), and as well as J. Chlasta for his help in adapting the MARS protocol to follicles. We are very grateful to A. Guichet, D. Bilder, Anne Ephrussi, J.R. Huynh, B. Loppin, Sally Horne-Badovinac for flies, V. Van de Bor for flies and discussion. We acknowledge X. Wang for critical comments on the manuscript.

Competing interests

No competing interests declared.

Funding

This work is supported by the ANR (Blanc 12-SVSE-0023-01, MechInMorph), the Centre National pour la Recherche Scientifique and the Ecole Normale Supérieure of Lyon.

References

Alsous, J., Villoutreix, P., Berezhkovskii, A.M., and Shvartsman, S.Y. (2017). Collective Growth in a Small Cell Network. Curr. Biol.

Bangi, E., and Wharton, K. (2006). Dpp and Gbb exhibit different effective ranges in the establishment of the BMP activity gradient critical for Drosophila wing patterning. Dev. Biol. *295*, 178–193.

Beauzamy, L., Derr, J., and Boudaoud, A. (2015). Quantifying hydrostatic pressure in plant cells by using indentation with an atomic force microscope. Biophys. J. *108*, 2448–2456.

Berutti, E. et al. (2012). Root canal anatomy preservation of waveone reciprocating files with or without glide path. J. Endod.

Brigaud, I., Duteyrat, J.-L., Chlasta, J., Bail, S.L., Couderc, J.-L., and Grammont, M. (2015). Transforming growth factor b/activin signalling induces epithelial cell flattening during drosophila oogenesis. Biol. Open *4*.

Butler, L.C., et al. (2009). Cell shape changes indicate a role for extrinsic tensile forces in Drosophila germ-band extension. Nat. Cell Biol. *11*, 859–864.

Chlasta, J., Milani, P., Runel, G., Duteyrat, J.-L., Arias, L., Lamiré, L.-A., Boudaoud, A., and Grammont, M. (2017). Variations in basement membrane mechanics are linked to epithelial morphogenesis. Dev. *144*.

Compagnon, J., Gervais, L., Roman, M.S., Chamot-Boeuf, S., and Guichet, A. (2009). Interplay between Rab5 and PtdIns(4,5)P2 controls early endocytosis in the Drosophila germline. J. Cell Sci. *122*, 25–35.

Coutelis, J.-B., and Ephrussi, A. (2007). Rab6 mediates membrane organization and determinant localization during Drosophila oogenesis. Development.

Crest, J., Diz-Muñoz, A., Chen, D.Y., Fletcher, D.A., and Bilder, D. (2017). Organ sculpting by patterned extracellular matrix stiffness. Elife *6*, 1–16.

Daley, W.P., and Yamada, K.M. (2013). ECM-modulated cellular dynamics as a driving force for tissue morphogenesis. Curr. Opin. Genet. Dev. *23*, 408–414.

Denef, N., Chen, Y., Weeks, S.D., Barcelo, G., and Schüpbach, T. (2008). Crag regulates epithelial architecture and polarized deposition of basement membrane proteins in Drosophila. Dev. Cell *14*, 354–364.

Díaz de la Loza, M.C., et al. (2017). Laminin Levels Regulate Tissue Migration and Anterior-Posterior Polarity during Egg Morphogenesis in Drosophila. Cell Rep. *20*, 211–223.

Etournay, R. et al. (2015). Interplay of cell dynamics and epithelial tension during morphogenesis of the Drosophila pupal wing. Elife *4*, 1–51.

Farge, E. (2003). Mechanical induction of Twist in the Drosophila foregut/stomodeal primordium. Curr. Biol.

Farhadifar, R., Röper, J.C., Aigouy, B., Eaton, S., and Jülicher, F. (2007). The Influence of Cell Mechanics, Cell-Cell Interactions, and Proliferation on Epithelial Packing. Curr. Biol. *17*, 2095–2104.

Fernandez, R., Das, P., Mirabet, V., Moscardi, E., Traas, J., Verdeil, J.-L., Malandain, G., and Godin, C. (2010). Imaging plant growth in 4D: robust tissue reconstruction and lineaging at cell resolution. Nat. Methods *7*, 547–553.

Fischer, R.S., Gardel, M., Ma, X., Adelstein, R.S., and Waterman, C.M. (2009).

Report Local Cortical Tension by Myosin II Guides 3D Endothelial Cell Branching. Curr. Biol. *19*, 260–265.

Fletcher, G.C., Diaz-De-La-Loza, M.-D.-C., Borreguero-Mun˜ Oz, N., Holder, M., Aguilar-Aragon, M., and Thompson, B.J. (2018). Mechanical strain regulates the Hippo pathway in Drosophila.

Golic, K.G., and Lindquist, S. (1989). The FLP recombinase of yeast catalyzes site-specific recombination in the drosophila genome. Cell *59*, 499–509.

Gomez, J.M., Wang, Y., and Riechmann, V. (2012). Tao controls epithelial morphogenesis by promoting fasciclin 2 endocytosis. J. Cell Biol. *199*, 1131–1143.

Grammont, M. (2007). Adherens junction remodeling by the Notch pathway in Drosophila melanogaster oogenesis. J. Cell Biol. *177*.

Haigo, S.L., and Bilder, D. (2011). Global Tissue Revolutions in a Morphogenetic Movement Controlling Elongation. Science (80-.). *331*, 1071–1074.

He, L., Wang, X., Tang, H.L., and Montell, D.J. (2010). Tissue elongation requires oscillating contractions of a basal actomyosin network. Nat. Cell Biol. *12*, 1133–1142.

Heer, N.C., and Martin, A.C. (2017). Tension, contraction and tissue morphogenesis. Development *144*, 4249–4260.

Hiramatsu, R., Matsuoka, T., Kimura-Yoshida, C., Han, S.W., Mochida, K., Adachi, T., Takayama, S., and Matsuo, I. (2013). External mechanical cues trigger the establishment of the anterior-posterior axis in early mouse embryos. Dev. Cell *27*, 131–144.

Hoffman, B.D., and Yap, A.S. (2015). Towards a Dynamic Understanding of Cadherin-Based Mechanobiology. Trends Cell Biol. *25*, 803–814.

Huang, J., Zhou, W., Dong, W., Watson, A.M., and Hong, Y. (2009). From the Cover: Directed, efficient, and versatile modifications of the Drosophila genome by genomic engineering. Proc. Natl. Acad. Sci. U. S. A. *106*, 8284–8289.

Hutter, J., and Bechhoefer, J. (1993). Calibration of atomic force microscope tips. Rev. Sci. Instrum. *64*, 1868.

Isabella, A.J., and Horne-Badovinac, S. (2015). Dynamic regulation of basement membrane protein levels promotes egg chamber elongation in Drosophila. Dev. Biol. *406*, 212–221.

Isabella, A.J., and Horne-Badovinac, S. (2016). Rab10-Mediated Secretion Synergizes with Tissue Movement to Build a Polarized Basement Membrane Architecture for Organ Morphogenesis. Dev. Cell *38*, 47–60.

Ito, K., Sass, H., Urban, J., Hofbauer, A., and Schneuwly, S. (1997). GAL4-responsive UAS-tau as a tool for studying the anatomy and development of the Drosophila central nervous system. Cell Tissue Res.

Janmey, P.A., Georges, P.C., and Hvidt, S. (2007). Basic Rheology for Biologists. Methods Cell Biol. *83*.

Kasza, K.E., Rowat, A.C., Liu, J., Angelini, T.E., Brangwynne, C.P., Koenderink, G.H., and Weitz, D.A. (2007). The cell as a material. Curr. Opin. Cell Biol. *19*, 101–107.

Kim, S.N., Jeibmann, A., Halama, K., Witte, H.T., Walte, M., Matzat, T., Schillers, H., Faber, C., Senner, V., Paulus, W., et al. (2014). ECM stiffness regulates glial migration in Drosophila and mammalian glioma models. Development *141*, 3233–3242.

King, R.C. (1970). Ovarian development in Drosophila melanogaster. Acad. Press.

Kolahi, K.S., White, P.F., Shreter, D.M., Classen, A.K., Bilder, D., and Mofrad, M.R.K. (2009). Quantitative analysis of epithelial morphogenesis in Drosophila oogenesis: New insights based on morphometric analysis and mechanical modeling. Dev. Biol. *331*, 129–139.

Lerner, D.W., McCoy, D., Isabella, A.J., Mahowald, A.P., Gerlach, G.F., Chaudhry, T.A., and Horne-Badovinac, S. (2013). A Rab10-Dependent Mechanism for Polarized Basement Membrane Secretion during Organ Morphogenesis. Dev. Cell *24*, 159–168.

Lévy, R., and Maaloum, M. (2002). Measuring the spring constant of atomic force microscope cantilevers: thermal fluctuations and other methods. Nanotechnology *13*, 33–37.

Li, M.A., Alls, J.D., Avancini, R.M., Koo, K., and Godt, D. (2003). The large Maf factor Traffic Jam controls gonad morphogenesis in Drosophila. Nat. Cell Biol. *5*, 994–1000.

Lohs-Schardin, M. (1982). Dicephalic-A Drosophila Mutant Affecting Polarity in Follicle Organization and Embryonic Patterning. Wilhelm Roux Arch. Dev. Biol.. *191*.

Mammoto, T., and Ingber, D.E. (2010). Mechanical control of tissue and organ development. Development *137*, 1407–1420.

Martin, A.C., Kaschube, M., and Wieschaus, E.F. (2009). Pulsed contractions of an actin–myosin network drive apical constriction. Nature *457*, 495–499.

Mata, J., Curado, S., and Ephrussi, A. (2000). Tribbles coordinates mitosis and morphogenesis in Drosophila by regulating String/CDC25 proteolysis. Cell *101*,

511_522.
Mesmoudi, M.M., Floriani, L. De, and Magillo, P. (2010). A Geometric Aproach to Curvature Estimation on Triangulated 3D Shapes. Int. Conf. Comput. Graph. Theory Appl.
Michael, M., and Yap, A.S. (2013). The regulation and functional impact of actin assembly at cadherin cell-cell adhesions. Semin. Cell Dev. Biol. *24*, 298–307.
Milani, P., Mirabet, V., Cellier, C., Rozier, F., Hamant, O., Das, P., and Boudaoud, A. (2014). Matching Patterns of Gene Expression to Mechanical Stiffness at Cell Resolution through Quantitative Tandem Epifluorescence and Nanoindentation. Plant Physiol. *165*, 1399–1408.
Morin, X., Daneman, R., Zavortink, M., and Chia, W. (2001). A protein trap strategy to detect GFP-tagged proteins expressed from their endogenous loci in Drosophila. Proc. Natl. Acad. Sci. *98*, 15050–15055.
Murthy, M. (2003). The exocyst component Sec5 is required for membrane traffic and polarity in the Drosophila ovary. Development.
Ng, M.R. osa, Besser, A., Brugge, J.S., and Danuser, G. (2014). Mapping the dynamics of force transduction at cell-cell junctions of epithelial clusters. Elife *3*, e03282.
Oh, H., and Irvine, K.D. (2011). Cooperative Regulation of Growth by Yorkie and Mad through bantam.
Petrella, L.N., Smith-Leiker, T., and Cooley, L. (2007). The Ovhts polyprotein is cleaved to produce fusome and ring canal proteins required for Drosophila oogenesis. Development.
Pilot, F., Philippe, J.-M., Lemmers, C., and Lecuit, T. (2006). Spatial control of actin organization at adherens junctions by a synaptotagmin-like protein. Nature *442*, 580–584.
Prasad, M., and Montell, D.J. (2007). Cellular and Molecular Mechanisms of Border Cell Migration Analyzed Using Time-Lapse Live-Cell Imaging. Dev. Cell *12*, 997–1005.
Quintin, S., Gally, C., and Labouesse, M. (2008). Epithelial morphogenesis in embryos: asymmetries, motors and brakes. Trends Genet. *24*, 221–230.
Rauskolb, C., Sun, S., Sun, G., Pan, Y., and Irvine, K.D. (2014). Cytoskeletal tension inhibits Hippo signaling through an Ajuba-Warts complex. Cell *158*, 143–156.
Rauzi, M., Verant, P., Lecuit, T., and Lenne, P.-F. (2008). Nature and anisotropy of

cortical forces orienting Drosophila tissue morphogenesis. Nat. Cell Biol. *10*, 1401–1410.

Ridler, T.W. Calvard, S. (1978). Picture Thresholding Using an Iterative Slection Method. IEEE Trans. Syst. Man Cybern.

Robinson, D.N., Cant, K., and Cooley, L. (1994). Morphogenesis of Drosophila ovarian ring canals. Development *120*, 2015–2025.

Schneider, C.A., Rasband, W.S., and Eliceiri, K.W. (2012). NIH Image to ImageJ: 25 years of Image Analysis HHS Public Access.

Schneider, M., Khalil, A. a, Poulton, J., Castillejo-Lopez, C., Egger-Adam, D., Wodarz, A., Deng, W.-M., and Baumgartner, S. (2006). Perlecan and Dystroglycan act at the basal side of the Drosophila follicular epithelium to maintain epithelial organization. Development *133*, 3805–3815.

Spradling., A.C. (1993). Developmental genetics of oogenesis. In *The Development of Drosophila Melanogaster*, p.

Stewart, M.P., Helenius, J., Toyoda, Y., Ramanathan, S.P., Muller, D.J., and Hyman, A.A. (2011). Hydrostatic pressure and the actomyosin cortex drive mitotic cell rounding. Nature *469*, 226–230.

Taylor- Weiner, H., Ravi, N., and Engler, A.J. (2015). Traction forces mediated by integrin signaling are necessary for definitive endoderm specification. J. Cell Sci. *128*, 1961–1968.

Tseng, Q., Duchemin-Pelletier, E., Deshiere, A., Balland, M., Guillou, H., Filhol, O., and Thery, M. (2012). Spatial organization of the extracellular matrix regulates cell-cell junction positioning. Proc. Natl. Acad. Sci.

Vella, D., Ajdari, A., Vaziri, A., and Boudaoud, A. (2012). Indentation of ellipsoidal and cylindrical elastic shells. Phys. Rev. Lett.

Viktorinová, I., and Dahmann, C. (2013). Microtubule polarity predicts direction of egg chamber rotation in Drosophila. Curr. Biol. *23*, 1472–1477.

Xu, T., and Rubin, G.M. (1993). Analysis of genetic mosaics in developing and adult Drosophila tissues. Development.

Xu, K., Sacharidou, A., Fu, S., Chong, D.C., Skaug, B., Chen, Z.J., Davis, G.E., and Cleaver, O. (2011). Blood Vessel Tubulogenesis Requires Rasip1 Regulation of GTPase Signaling. Dev. Cell *20*, 526–539.

Xue, F., and Cooley, L. (1993). Kelch encodes a component of intercellular bridges in Drosophila egg chambers. Cell *72*, 681–693.

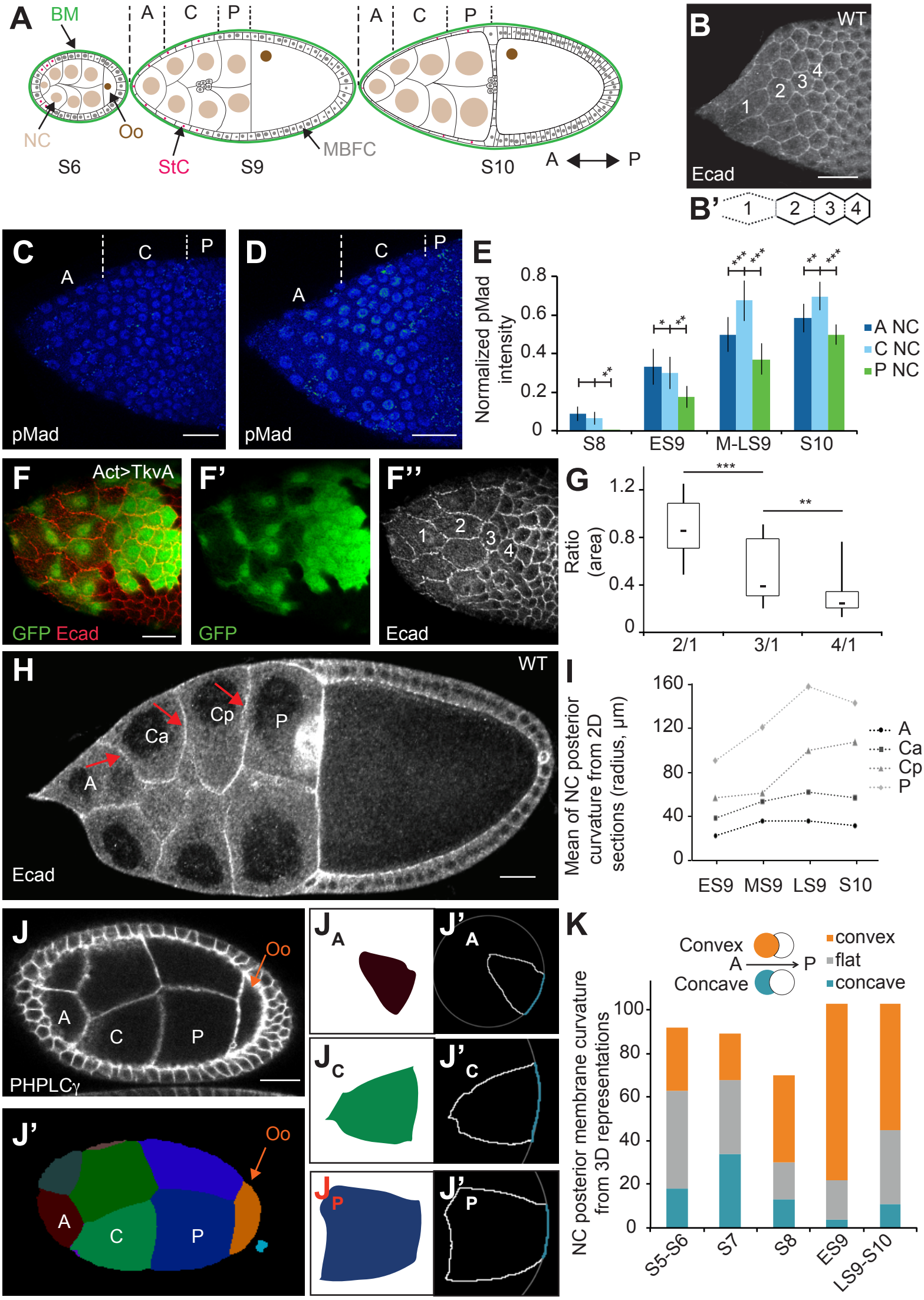
A
BM
A
C
P
A
C
P
NC
Oo
StC
MBFC
S6
S9
S10
A
P
B
WT
1
2
3
4
Ecad
B'
1
2
3
4
C
A
C
P
pMad
D
A
C
P
pMad
E
Normalized pMad intensity
0.8
0.6
0.4
0.2
0
S8
ES9
M-LS9
S10
A NC
C NC
P NC
F
Act>TkvA
GFP Ecad
F'
GFP
F''
1
2
3
4
Ecad
G
Ratio (area)
1.2
0.8
0.4
0
2/1
3/1
4/1
H
WT
Ca
Cp
P
A
Ecad
I
Mean of NC posterior curvature from 2D sections (radius, µm)
160
120
80
40
0
ES9
MS9
LS9
S10
A
Ca
Cp
P
J
Oo
A
C
P
PHPLCγ
J'
Oo
A
C
P
J A
J' A
J C
J' C
J P
J' P
K
Convex
A
P
Concave
convex
flat
concave
NC posterior membrane curvature from 3D representations
100
80
60
40
20
0
S5-S6
S7
S8
ES9
LS9-S10

Figure 1: Nurse cell geometry indicates an A/P gradient of inner pressure.

In all Figures, anterior is to the left. (A) Schematic representation of an ovariole with a germarium and follicles at three different developmental stages (S6, S9 and S10) with nurse cells (NCs), oocyte (Oo), main body follicular cells (MBFC), stretched cells (StCs) and basement membrane (BM) indicated. From S8 onwards, NCs are grouped into three regions for analysis: anterior (A), central (C) and the four posterior (P) NCs. (B) Adherens junctions (Ecad) remodelling in a S9 follicle. Four cells are labelled from anterior (1) to posterior (4) to highlight the progressive decrease of apical surface. (B') Schematic representation of AJ remodelling, with dotted lines representing remodelled AJs and solid lines representing intact AJs. (C, D) pMad expression in early (C) and mid (D) WT S9 follicles. The A, C and P regions of the NCs are indicated. (E) Quantification of pMad in follicular cells during StC flattening (n > 15 nuclei per condition). (F) TkvA-expressing StCs in a S9 follicle marked by GFP (F and F'), and with StCs labelled in decreasing order of apical surface area (F''). (G) Box and whisker plot of the ratio of surface area between TkvA-expressing StCs at the different positions shown in F'' (n > 23 cells per plot). (H) A late S9 follicle showing the curvature of the membranes (arrows) between the anterior (A) and a central NC (Ca), between two central NCs (Ca and Cp), or between a central (Cp) and a posterior (P) NC. Ca and Cp refer to a central NC in contact with an anterior NC or a posterior NC, respectively. (I) Mean of the NC posterior membrane curvatures (as labelled in H) at either early-S9 (ES9; n = 98 cells), mid S9 (MS9; 42 cells), late S9 (LS9; 25 cells) or S10 (S10; 15 cells). (J) A S8 follicle and the corresponding section from a 3D segmentation of the same (J') with NCs labelled from anterior to posterior. J_A, J_C and J_P correspond to slices showing the largest area for each labelled NC. J'_A, J'_C and J'_P show the outline (solid white line) of each cell, as well as the circle (dotted white line) fitted to the posterior membrane (blue line). (K) Number of convex (orange), flat (grey) and concave (blue) NC posterior membrane curvatures at different follicular stages (2 - 3 follicles per stage were reconstructed). Scale bars: 20 µm.

In box and whisker plots in all figures, boxes extend from 25 to 75 percentile, with a line showing the median value. Whiskers extend to the most extreme values. In all figures, *, ** and *** correspond to $p<0.5$, $p<0.05$ and $p<0.01$ (t-test), respectively.

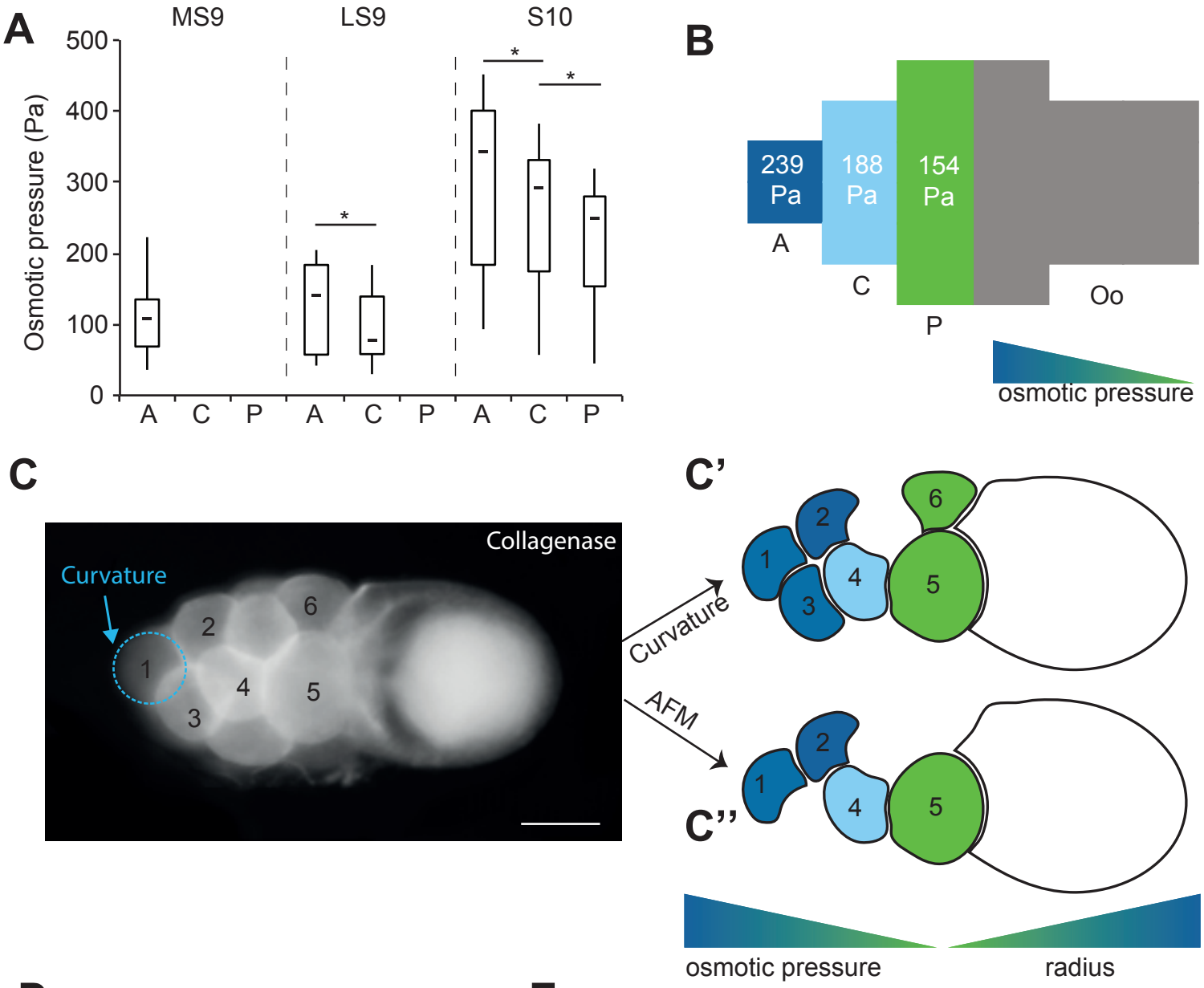
A
MS9
LS9
S10
Osmotic pressure (Pa)
500
400
300
200
100
0
A C P A C P A C P
*
*
*
B
239 Pa
188 Pa
154 Pa
A
C
P
Oo
osmotic pressure
C
Collagenase
Curvature
1
2
3
4
5
6
C'
Curvature
AFM
C''
osmotic pressure
radius

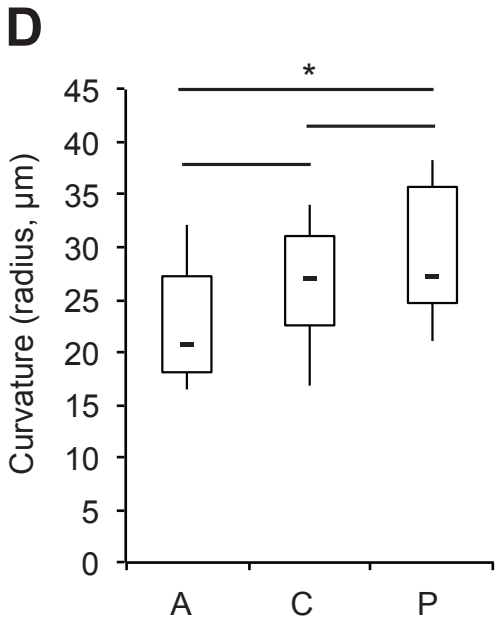
D
Curvature (radius, µm)
45
40
35
30
25
20
15
10
5
0
A C P
*

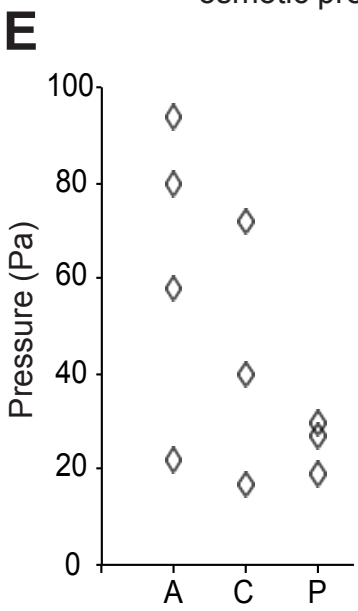
E
Pressure (Pa)
100
80
60
40
20
0
A C P

Figure 2. Nurse cell mechanical properties reveal an A/P gradient of inner pressure.

(A) Box and whisker plot of inner pressure in anterior (A), central (C) and posterior (P) NCs, from mid S9 (MS9) to S10 (S10) WT follicles (n > 10 per bar per stage). (B) Schematic representation of mean inner pressure in each region of WT S10 follicles, with a color-coded gradient from blue (high) to green (low). (C) A WT S10 follicle after collagenase treatment, showing the NCs bulging outwards, with the corresponding schematic representation of the pressure gradient based on NC membrane curvature (the measured curvature corresponds to the membrane bulging outwards) (C') or based on AFM measurements (C''). (D) Box and whisker plot of the radius of curvature of A, C or P NCs (n > 20 per region). (E) AFM measurements of inner pressure in A, C or P NCs after collagenase treatment. Scale bar: 50 µm.

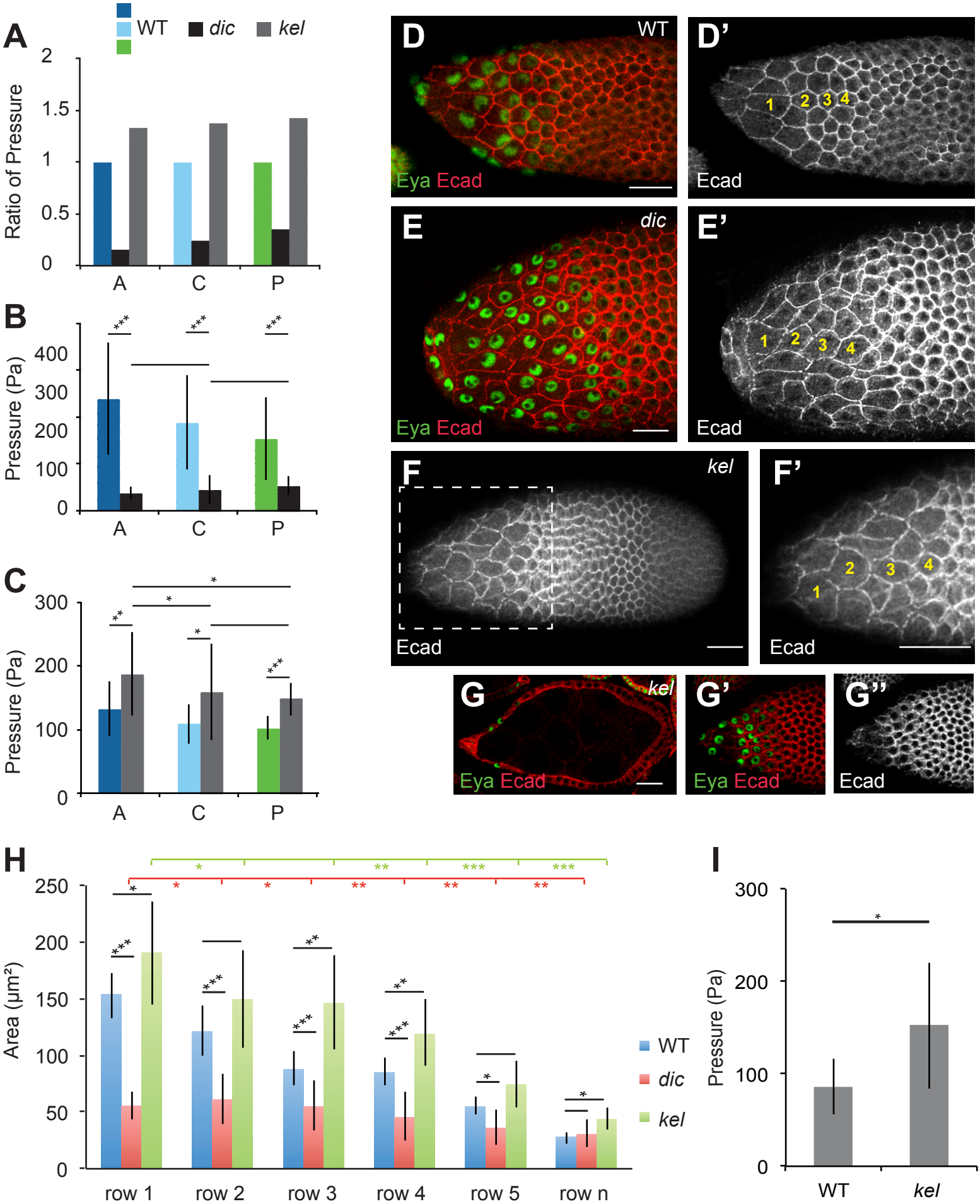
A
WT
dic
kel
Ratio of Pressure
2
1.5
1
0.5
0
A
C
P
B
Pressure (Pa)
400
300
200
100
0
***
C
Pressure (Pa)
300
200
100
0
*
**
D
WT
Eya Ecad
D'
1
2
3
4
Ecad
E
dic
Eya Ecad
E'
Ecad
F
kel
Ecad
F'
Ecad
G
kel
Eya Ecad
G'
Eya Ecad
G''
Ecad
H
Area (µm²)
250
200
150
100
50
0
row 1
row 2
row 3
row 4
row 5
row n
WT
dic
kel
I
Pressure (Pa)
300
200
100
0
WT
kel

Figure 3: The gradient of NC inner pressure controls the timing and the wave of stretched cell flattening

(A) Ratio of pressure in S10 A, C or P NCs between *dic*, *kel* and WT. (B) Inner pressure of S10 A, C or P NCs between *dic* and WT (n > 15 for WT, n = 5 for *dic*). (C) Inner pressure of at S10 A, C or P NCs between *kel* and WT (n > 10 for WT, n = 7 for *kel*). Note that WT values in B and C are specific to each experiment (see Methods). (D-E) StC flattening in mid S9 WT (D) or *dic* (E) follicles. (F, G) Stage 8 *kel* follicles displaying premature StC flattening. Surface views (F, G, G'') of the follicle or view across the follicle (G); F' is a magnified view of the box drawn in F. For D-F, four cells are numbered in yellow along the A/P axis. For staging *dic* or *kel* follicles, see methods. (H) Apical StC surface area by position along the A/P axis in WT (blue), *dic* (red) or *kel* (green) mid S9 follicles (n > 10 cells for each row). Statistical comparisons between WT and *dic* or WT and *kel* are indicated in black, between *dic* rows in red and between *kel* rows in green. (I) Inner pressure of WT and *kel* anterior NCs in mid S9 follicles (n=12 for WT, n=7 for *kel*). Scale bar: 20 µm.

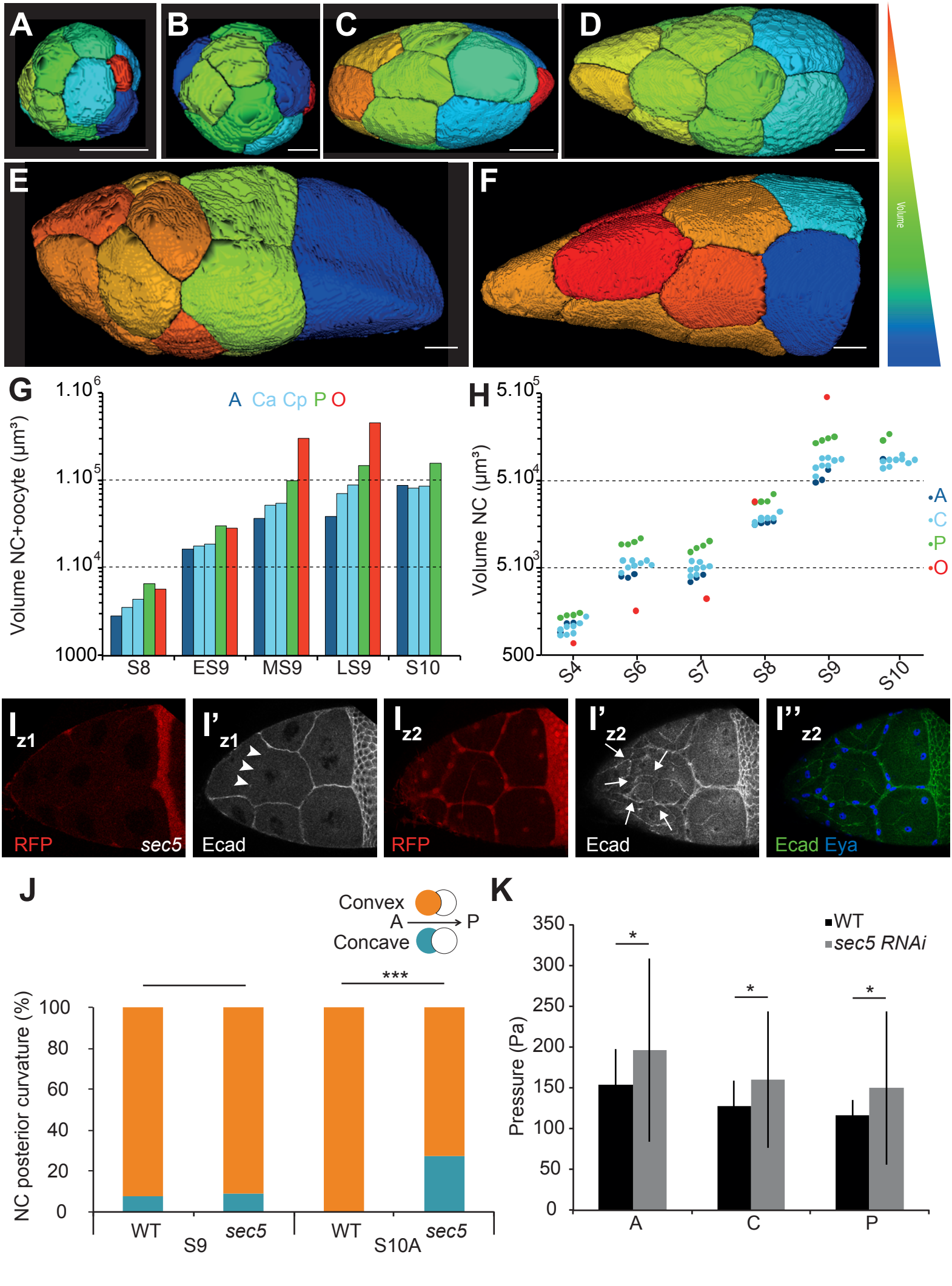
A
B
C
D
E
F
Volume
G
A Ca Cp P O
Volume NC+oocyte (µm³)
1.10^6
1.10^5
1.10^4
1000
S8
ES9
MS9
LS9
S10
H
Volume NC (µm³)
5.10^5
5.10^4
5.10^3
500
S4
S6
S7
S8
S9
S10
A
C
P
O
I z1
RFP
sec5
I' z1
Ecad
I z2
RFP
I' z2
Ecad
I'' z2
Ecad Eya
J
Convex
A
P
Concave
***
NC posterior curvature (%)
100
80
60
40
20
0
WT
sec5
S9
WT
sec5
S10A
K
WT
sec5 RNAi
Pressure (Pa)
350
300
250
200
150
100
50
0
*
*
*
A
C
P

Figure 4: Intrinsic nurse cell growth is important for the pressure gradient.

(A-F) 3D reconstructions of germline cells in WT follicles at S7 (A), S8 (B), early S9 (C), mid S9 (D), late S9 (E) and S10 (F). Only NCs, but not the oocyte, are shown in F. The arbitrary color-scale indicates relative cell volumes for each follicle. (G) Volumes of A (dark blue), C (light blue) and P (green) NC and the oocyte (red) from S8 to S10 WT follicles. C NCs are further subdivided into those abutting the A NC (Ca) and those abutting the four P NC (Cp). (H) Individual NC volumes for each measured follicle. (I) Anterior part of a S10 follicle with a germline clone for $Sec5^{E13}$ (marked by the absence of RFP) with a focus either on NCs (z1) or on StCs (z2). White arrowheads (I'_{z1}) and arrows (I'_{z2}) indicate a missing NC membrane or intact AJ, respectively. (J) NC posterior membrane curvatures in S9 and S10A WT and *Sec5* follicles, showing the percentage with convex (orange) or concave (blue) curvatures (n > 10). (K) Inner pressure of A, C and P NCs in S10 WT and *Sec5* RNAi follicles (n > 10).

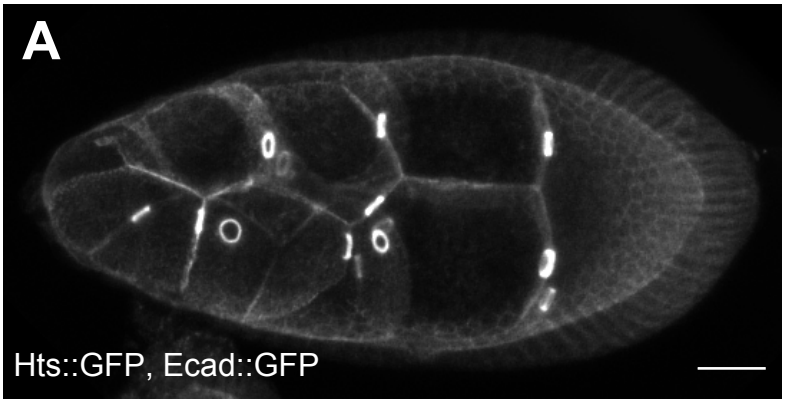
A
Hts::GFP, Ecad::GFP

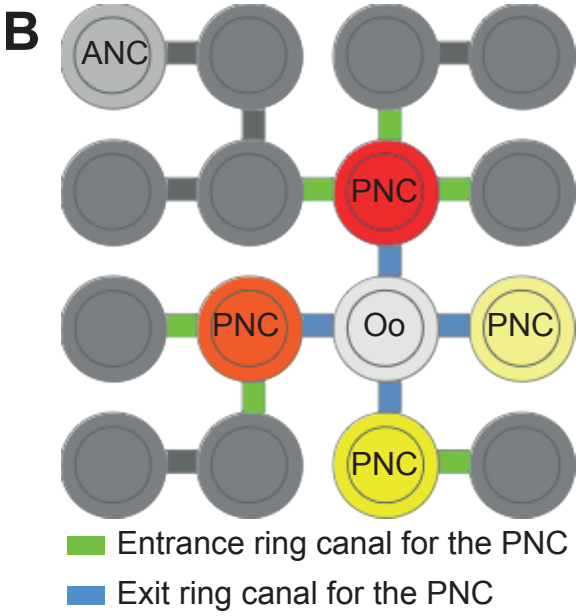
B
ANC
PNC
PNC
Oo
PNC
PNC
Entrance ring canal for the PNC
Exit ring canal for the PNC

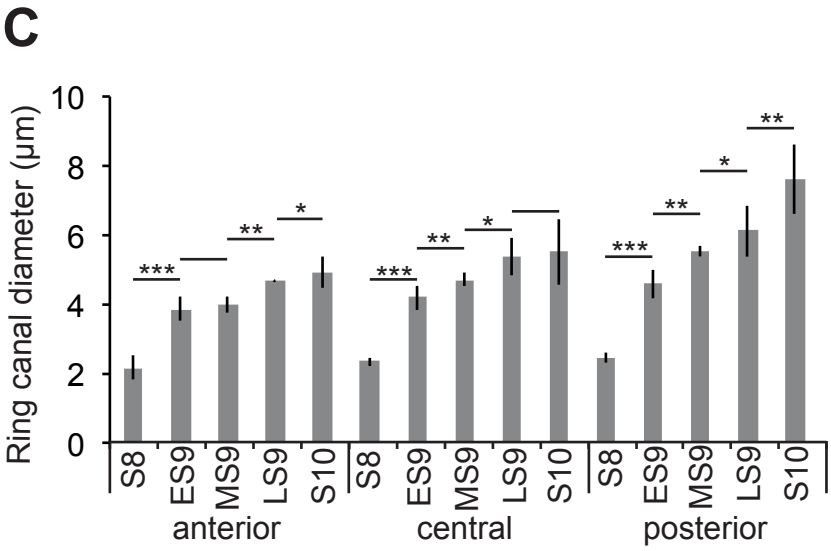
C
Ring canal diameter (µm)
10
8
6
4
2
0
***
**
*
***
**
*
***
**
*
**
S8
ES9
MS9
LS9
S10
S8
ES9
MS9
LS9
S10
S8
ES9
MS9
LS9
S10
anterior
central
posterior

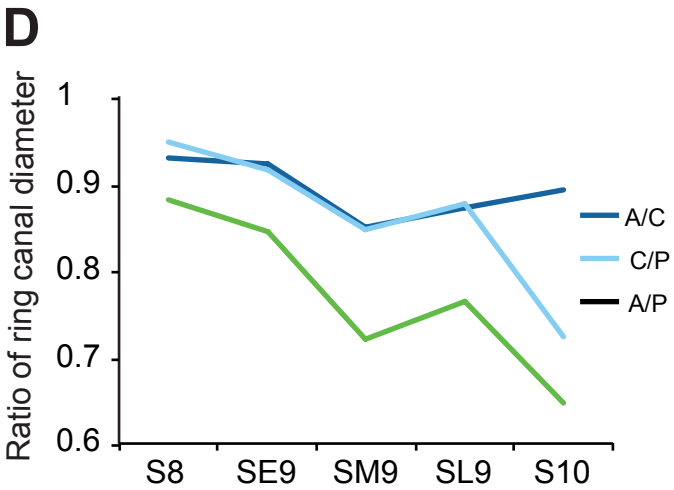
D
Ratio of ring canal diameter
1
0.9
0.8
0.7
0.6
S8
SE9
SM9
SL9
S10
A/C
C/P
A/P

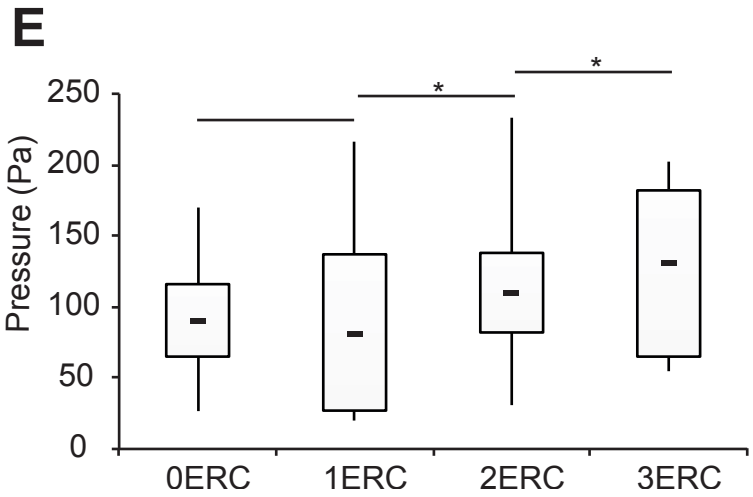
E
Pressure (Pa)
250
200
150
100
50
0
*
*
0ERC
1ERC
2ERC
3ERC

Figure 5: Establishment of a pressure gradient depends on nurse cell ring canals.

(A) A S9 follicle showing the RCs between the NCs. (B) Schematic representation of the 16 germline cells and their stereotypic connections through RCs The anteriormost NC (ANC) is shown in light grey. The four posterior NCs (PNCs, red or yellow) connect to the oocyte (Oo; white) via the RCs shown in blue. One PNC (light yellow) has no ERC, while the three others have one, two or three ERC (green). (C) Quantification of RC inner diameters from S8 to S10 as a function of their A, C and P localisation (n = 5 per stage). (D) Ratios of RC diameters at different follicular stages. Ratios are presented for A-C NCs (dark blue), A-P NCs (green) or C-P NCs (light blue). (E) Box and whisker plot of inner pressure in the four posterior NCs as a function of the number of ERC (n > 10 for NCs with zero, one or two ERC and n = 5 for NCs with three ERC).

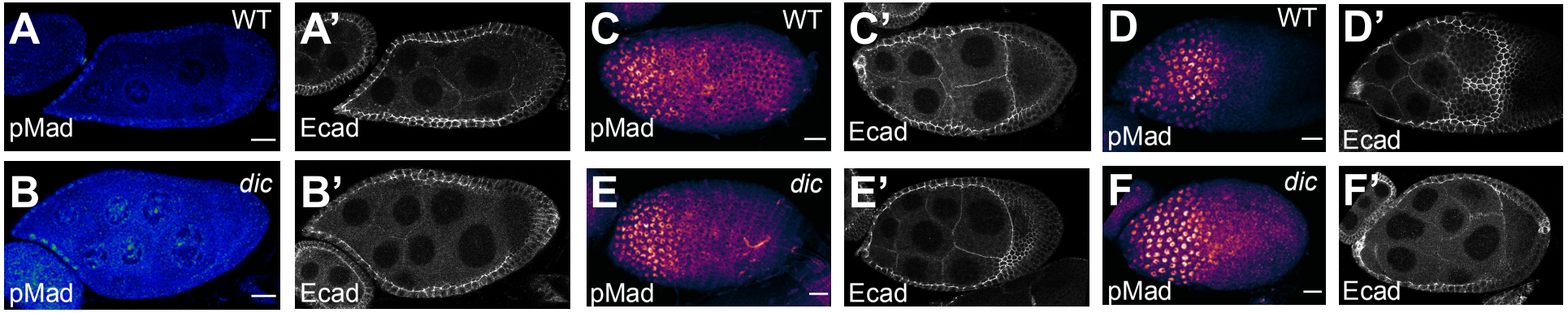
A
WT
pMad
A'
Ecad
C
WT
pMad
C'
Ecad
D
WT
pMad
D'
Ecad
B
dic
pMad
B'
Ecad
E
dic
pMad
E'
Ecad
F
dic
pMad
F'
Ecad

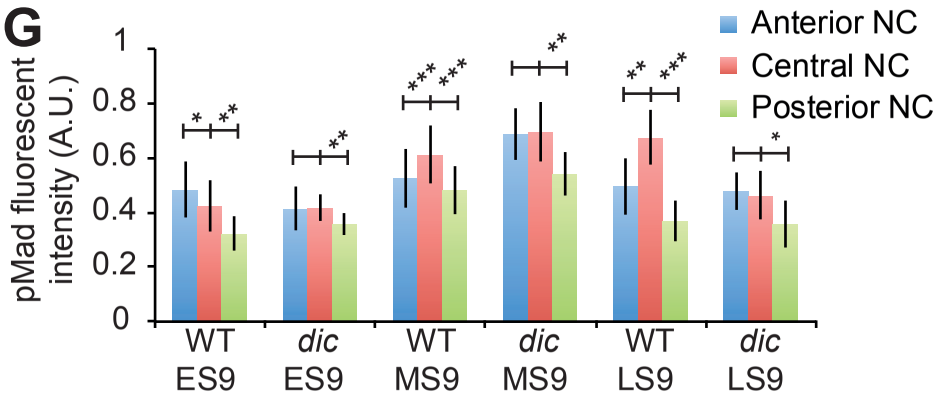
G
pMad fluorescent intensity (A.U.)
1
0.8
0.6
0.4
0.2
0
Anterior NC
Central NC
Posterior NC
WT ES9
dic ES9
WT MS9
dic MS9
WT LS9
dic LS9

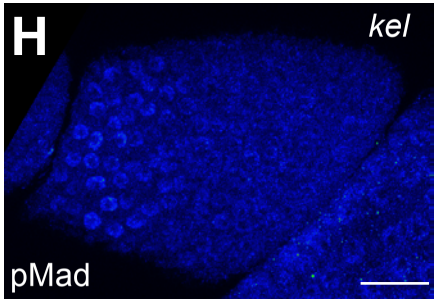
H
kel
pMad

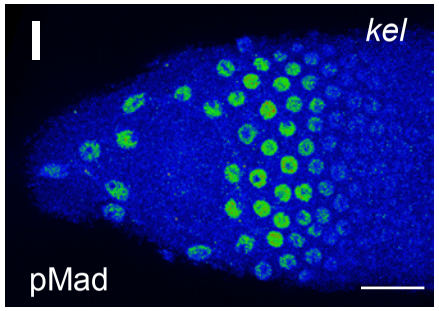
I
kel
pMad

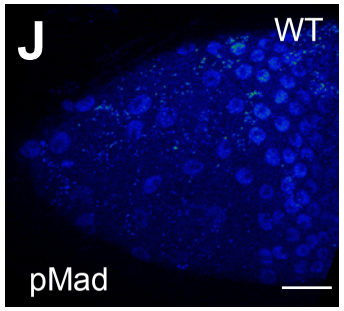
J
WT
pMad

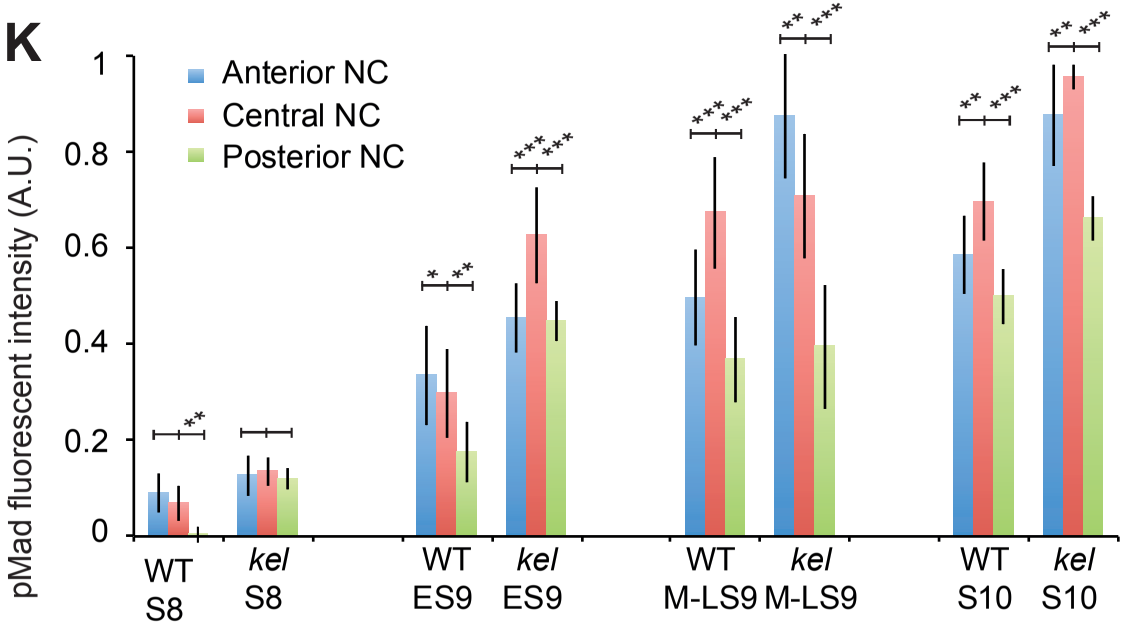
K
pMad fluorescent intensity (A.U.)
1
0.8
0.6
0.4
0.2
0
Anterior NC
Central NC
Posterior NC
WT S8
kel S8
WT ES9
kel ES9
WT M-LS9
kel M-LS9
WT S10
kel S10

Figure 6: The pressure gradient controls the timing and the activity of the TGFß pathway.

(A-B) Sections through a S8 WT (A) or a *dic* (B) follicles. For staging, see Methods. (C-F) Projections of the sections displaying pMad expression in the StCs in a WT early S9 (ES9) follicle (C), of a WT mid-S9 (MS9) follicle (D), of a *dic* early S9 follicle (E) or of a *dic* mid S9 follicle (F). (G) Quantification of pMad fluorescence in WT and *dic* follicles per stage (n > 15 nuclei per area). (H-J) Projections of the sections displaying pMad fluorescence in the StCs in a *kel* S7 follicle (H), in a *kel* mid S9 follicle (I) or in a WT mid S9 follicle (J). (K) Quantification of pMad fluorescence in WT and *kel* follicles per stage (n > 15 nuclei per region). Scale bar: 20 µm

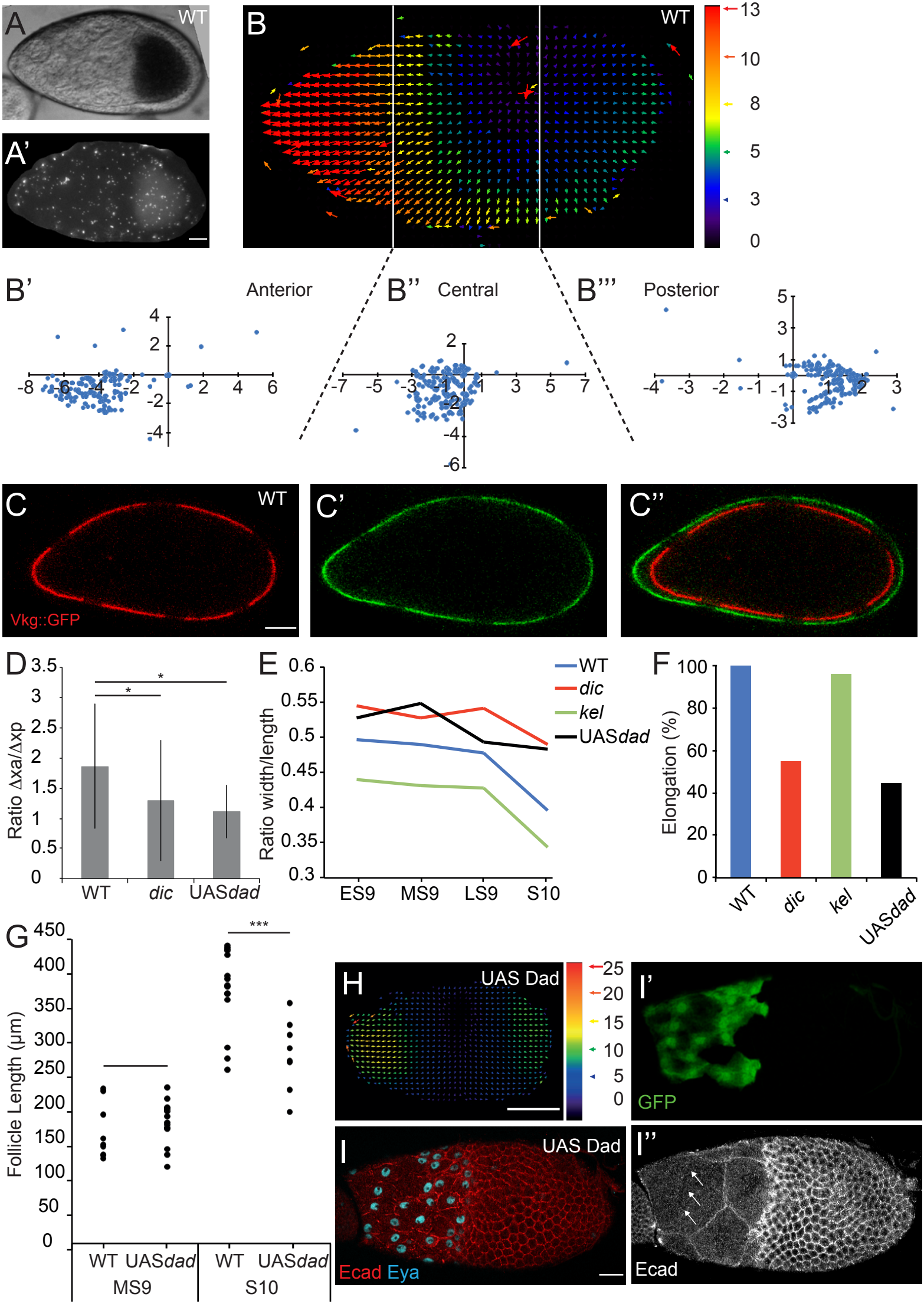
A
WT
A'
B
WT
13
10
8
5
3
0
B'
Anterior
B''
Central
B'''
Posterior
C
WT
Vkg::GFP
C'
C''
D
Ratio Δxa/Δxp
WT
dic
UASdad
E
Ratio width/length
ES9
MS9
LS9
S10
WT
dic
kel
UASdad
F
Elongation (%)
WT
dic
kel
UASdad
G
Follicle Length (µm)
WT
UASdad
MS9
WT
UASdad
S10
H
UAS Dad
I'
GFP
I
UAS Dad
Ecad Eya
I''
Ecad

Figure 7: The follicles grow more anteriorly than posteriorly at S9.

(A) A WT mid S9 follicle covered with fluorescent beads (A'). (B) Particle Image Velocimetry representation from the beads positioned on the follicle shown in A and plots presenting the coordinates of the vectors for the anterior (B'), central (B'') and posterior (B''') areas. For each area, the initial (x, y) coordinates of the beads are (0,0). Each blue dot corresponds to the final x and y coordinates of a bead. (C) WT mid S9 follicle from a female carrying the *vkg::GFP* transgene to mark the BM (red in C, green in C'). Six bleached areas are visible at t = o (C) and at t = 80 min (C'). The two images have been overlaid by aligning the central bleached areas (C'') to show follicle growth during the interval. (D) Box and whisker plot of the ratio between the anterior (xa) and posterior (xp) growths of the BM in WT (n=9), in *dic* follicles (n = 6) and in Dad-expressing follicles (n=5). (E) Evolution of the ratio between the width and the length of the follicles from early S9 to S10 (n > 20 per stage). (F) Percentage of follicle elongation at S10 in WT and mutant backgrounds. (G) Comparison of follicle length at mid S9 and at S10B between WT and Dad-expressing follicles (n > 20 per stage). (H) Particle Image Velocimetry representation from the beads positioned on a Dad-expressing follicle. (I) Section showing the Dad-expressing StCs (GFP) in a mid-S9 follicle (I'). Section of the follicle showing the breakage of a NC membrane (arrows) (I'').